JACS
JOURNAL OF THE AMERICAN CHEMICAL SOCIETY
pubs.acs.org/JACS
Article

Electrocatalytic Isoxazoline−Nanocarbon Metal Complexes

Shao-Xiong Lennon Luo, Richard Y. Liu, Sungsik Lee, and Timothy M. Swager*

Cite This: J. Am. Chem. Soc. 2021, 143, 10441−10453
Read Online
ACCESS | Metrics & More | Article Recommendations | Supporting Information

ABSTRACT: We report the synthesis of new carbon-nanomaterial-based metal chelates that enable effective electronic coupling to electrocatalytic transition metals. In particular, multiwalled carbon nanotubes (MWCNTs) and few-layered graphene (FLG) were covalently functionalized by a microwave-assisted cycloaddition with nitrile oxides to form metal-binding isoxazoline functional groups with high densities. The covalent attachment was evidenced by Raman spectroscopy, and the chemical identity of the surface functional groups was confirmed by X-ray photoelectron spectroscopy (XPS) and time-of-flight secondary ion mass spectrometry (ToF-SIMS). The functional carbon nanomaterials effectively chelate precious metals Ir(III), Pt(II), and Ru(III), as well as earth-abundant metals such as Ni(II), to afford materials with metal contents as high as 3.0 atom %. The molecularly dispersed nature of the catalysts was confirmed by X-ray absorption spectroscopy (XAS) and energy-dispersive X-ray spectroscopy (STEM-EDS) elemental mapping. The interplay between the chelate structure on the graphene surface and its metal binding ability has also been investigated by a combination of experimental and computational studies. The defined ligands on the graphene surfaces enable the formation of structurally precise heterogeneous molecular catalysts. The direct attachment of the isoxazoline functional group on the graphene surfaces provides strong electronic coupling between the chelated metal species and the conductive carbon nanomaterial support. We demonstrate that the metal-chelated carbon nanomaterials are effective heterogeneous catalysts in the oxygen evolution reaction with low overpotentials and tunable catalytic activity.

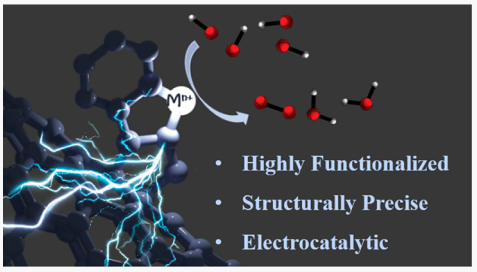

INTRODUCTION

Carbon nanomaterials, such as single-walled carbon nanotubes (SWCNTs), multiwalled carbon nanotubes (MWCNTs), and graphene, are an attractive class of materials with unique physical, mechanical, and electronic properties[1−8] that hold great potential in energy,[9−12] catalysis,[13−16] sensing,[17−23] and biomedical[24−28] applications. Pristine carbon nanomaterials lack the functionalities required for specific applications or processing, and as a result, extensive research efforts have targeted their functionalization.[29−34] These methods include noncovalent physisorbed attachments of small molecules and polymers to the surface by hydrophobic/$\pi-\pi$ interactions and covalent addition reactions with the edges, ends, or sidewalls.

We have endeavored to create robust methods for the attachment of transition-metal-binding ligands to create functional carbon nanomaterials for chemical sensing[35−38] and catalysis.[39−44] Our specific objectives are to create metal-functionalized nanomaterials that could maintain or enhance the expected activity of the metal species.[45,46] To this end, covalent attachment of multidentate metal chelates has been targeted to create nanostructures with predictable structures and properties. Metal chelation can provide access to heterogeneous molecular catalysts that possess both good electrochemical electron transfer properties and precise structural control at the molecular level.

In the present investigation we have focused on the attachment of metal chelates based on isoxazoline to graphene surfaces. As shown in Figure 1, the 2-pyridylisoxazole ring provides for a strong metal−carbon nanomaterial connection.

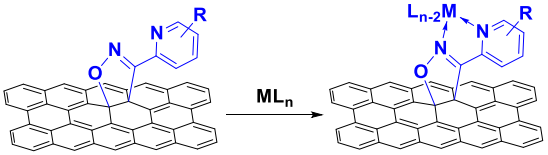

Figure 1. Schematic depiction of metal chelation by isoxazoline functional groups on the carbon nanomaterial surface.

The preconstructed chelating ligand provides for predictability of the metal complex structure, and the overlap of the ligand's p orbitals with the π-electronic states of the graphene surface allows for effective electronic coupling between a bound metal complex and the carbon nanomaterial.[47] Moreover, the distributed chelating ligands tend to stabilize low-nuclearity transition-metal compositions and thereby reduce the formation of aggregates and nanoparticles.[48,49] The isoxazoline

Received: May 26, 2021
Published: July 2, 2021

https://doi.org/10.1021/jacs.1c05439
J. Am. Chem. Soc. 2021, 143, 10441−10453

moiety can be effectively added to the graphene surfaces by 1,3-dipolar cycloadditions of nitrile oxides. Various kinds of carbon nanomaterials have been shown to undergo cycloaddition with nitrile oxides experimentally[50−52] and have also been studied computationally.[53] In this report, we apply this strategy to MWCNTs and few-layered graphene (FLG) to create a broad spectrum of transition-metal-functionalized carbon nanomaterials that serve as efficient heterogeneous molecular catalysts for the oxygen evolution reaction (OER), which is considered to be the bottleneck of the water-splitting process for clean energy conversion.[54−59] Furthermore, our complexation strategy is highly general and can be applied to many other important catalytic processes.

RESULTS AND DISCUSSION

We began our investigations by functionalizing MWCNTs with 2-pyridyl-, 2-pyrimidyl-, and 2,2′-bipyridylisoxazole rings. We have previously reported similar structures based on C_{60} that formed well-defined Re(I), Pt(II), and Ir(III) complexes.[47] The reactive nitrile oxide intermediates that we previously utilized can undergo a number of side reactions in addition to the functionalization of the nanomaterials. In the present one-pot procedure, we first generate nitrile oxide dimers by base treatment of *N*-hydroxyl imidoyl chlorides. Thermal cracking of these dimers local to the MWCNT surface is achieved by microwave irradiation of a dispersion in *o*-dichlorobenzene (*o*DCB). The high microwave absorptivity of MWCNTs provides for localized heating and has been shown to be a versatile method to effectively functionalize carbon nanomaterials.[60−66] In the present case this local heating generates the nitrile oxide groups proximate to the graphene surfaces. In our procedure, microwave irradiation serves two purposes: (a) it provides sufficient thermal energy for the *in situ* generation of the nitrile oxide reactive species via a retrocycloaddition of the preformed dimers[67,68] and (b) it locally activates the carbon nanomaterial surfaces and reactive intermediates. As shown in Scheme 1, this method can produce functionalized MWCNTs (**MWCNT-1**−**MWCNT-3**) containing bidentate or tridentate ligands for metal chelation.

The successful covalent modification on MWCNTs is revealed by Raman spectroscopy. Figure 2 shows the Raman spectra of pristine MWCNTs (**p-MWCNT**) and **MWCNT-1**−**MWCNT-3** under 633 nm laser excitation. Apart from the prominent G band (~1600 cm^{-1}) and D band (~1350 cm^{-1}), significant band broadening and higher spectral intensity in the valley between the G and D bands are observed. The latter is in part the result of the increase in satellite bands attributed to limit-sized sp^2 domains resulting from the covalent functionalization. Control experiments in the absence of nitrile oxide showed no change in Raman signals (Figure S1). By an

Scheme 1. Structures of Isoxazoline-Functionalized Multiwalled Carbon Nanotubes (MWCNTs)[a]

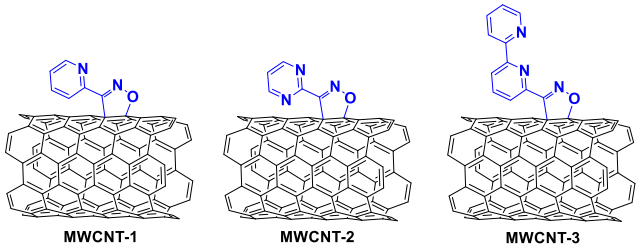

[a]MWCNTs are simplified as SWCNTs in the illustration for clarity.

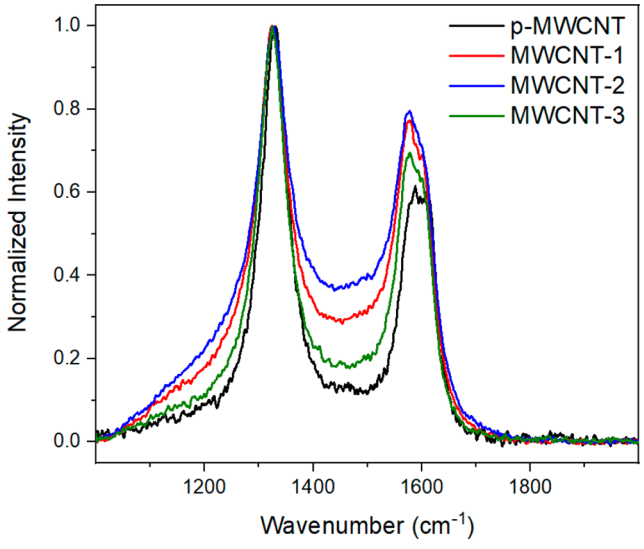

Figure 2. Raman spectra of **p-MWCNT** (black), **MWCNT-1** (red), **MWCNT-2** (blue), and **MWCNT-3** (green) collected with 633 nm laser excitation.

Table 1. Characterization of Functionalized MWCNTs

sample	Raman CFD	XPS composition (atom %) C 1s	N 1s	O 1s	weight loss at 800 °C (%)
p-MWCNT	0.40	98.8	0.0	1.2	2
MWCNT-1	1.14	86.9	7.5	5.6	14
MWCNT-2	1.15	80.3	13.5	6.2	31
MWCNT-3	0.58	90.4	4.9	4.7	12

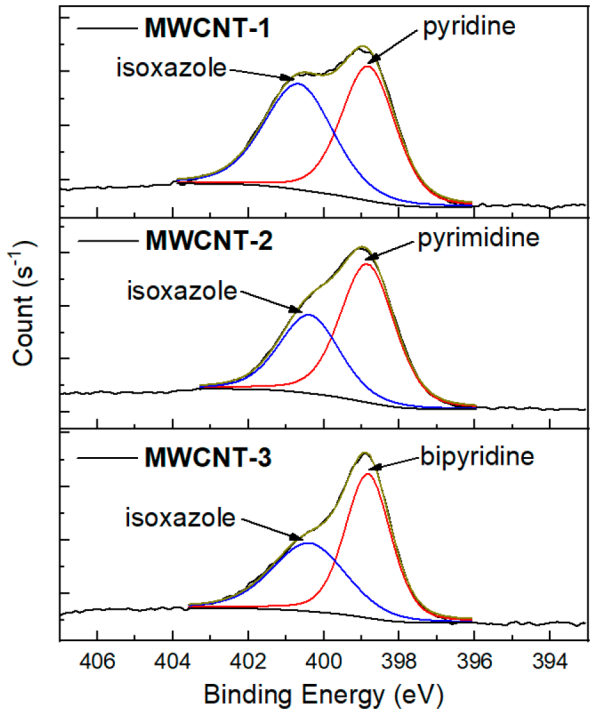

Figure 3. XPS N 1s spectra of **MWCNT-1** (top), **MWCNT-2** (middle), and **MWCNT-3** (bottom).

https://doi.org/10.1021/jacs.1c05439
J. Am. Chem. Soc. 2021, 143, 10441−10453

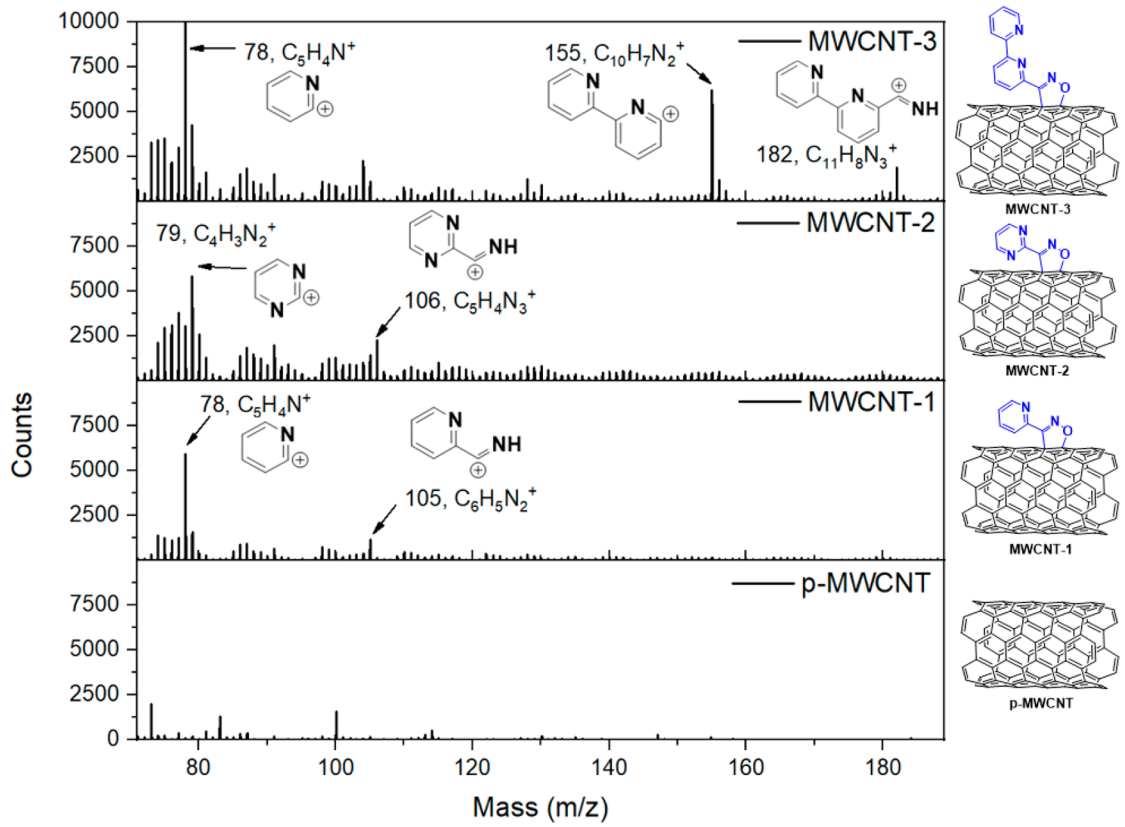

Figure 4. ToF-SIMS spectra of **p-MWCNT** and **MWCNT-1**−**MWCNT-3** in positive mode. MWCNTs are simplified as SWCNTs in the illustration for clarity.

Scheme 2. Synthesis of Isoxazoline-Functionalized Few-Layered Graphene

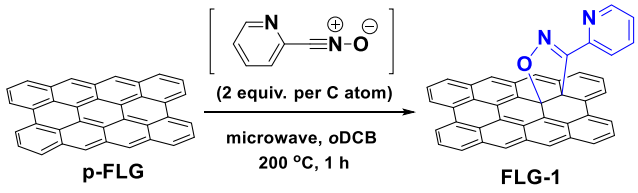

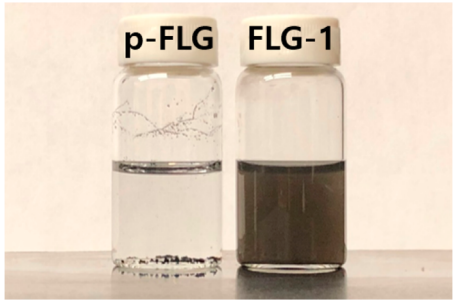

Figure 5. Photographs of dispersions of **p-FLG** (left) and **FLG-1** (right) in water (0.1 mg/mL).

established procedure,[69] detailed Raman peak deconvolution has been performed (Figure S2) and the Raman chemical functionalization degree (CFD) for the functionalized MWCNTs are shown in Table 1, reflecting the extent of covalent modification. Moreover, the G band peaks of the functionalized MWCNTs are shifted to lower wavenumbers in comparison to that of **p-MWCNT** (Figure S3), indicating the electronic effects of the surface functional groups on the MWCNTs.[70,71]

The chemical identity of the surface functional groups was analyzed by X-ray photoelectron spectroscopy (XPS). The XPS survey scans of the functionalized MWCNTs (Figures S4−S7) showed significant increase in nitrogen and oxygen content, as summarized in Table 1. Specifically, **MWCNT-1**−**MWCNT-3** are found to contain nitrogen at 7.5, 13.7, and 4.9 atom % and oxygen at 5.6, 6.2, and 4.7 atom %, respectively. To exclude the possibility of simple physisorption of functional groups, control experiments were performed where no heating was applied to generate the reactive nitrile oxide intermediate, and only minimal incorporation of nitrogen content was observed (Figure S8). High-resolution XPS spectra in the N 1s region are shown in Figure 3 and reveal the local environment of the nitrogen species present. Characteristic pyridinic N 1s peaks at around 398.6 eV[72] are found in all functionalized MWCNTs, and the isoxazole N 1s peaks are at around 400.4 eV.[53] Both signals are in agreement with the N 1s peaks observed in the small-molecule analogue $\mathbf{C_{60}}$**-1** reported previously (Figure S9).[47] The ratios of the two characteristic peaks agree with their anticipated atomic stoichiometry. As derived from the ratio between pyridinic N 1s and C 1s peaks, the degrees of functionalization were found to be 4.6, 5.6, and 1.6 functional groups per 100 CNT carbon atoms for **MWCNT-1**−**MWCNT-3**, respectively. These ratios are in agreement with the Raman CFD values (Figure S10).

In order to gain molecular-level structural information on the surface functional groups, the modified MWCNTs were analyzed by time-of-flight secondary ion mass spectrometry (ToF-SIMS), a highly sensitive surface analytical technique

https://doi.org/10.1021/jacs.1c05439
J. Am. Chem. Soc. 2021, 143, 10441−10453

Scheme 3. Metal Chelation Reactions of Isoxazoline-Functionalized MWCNTs[a]

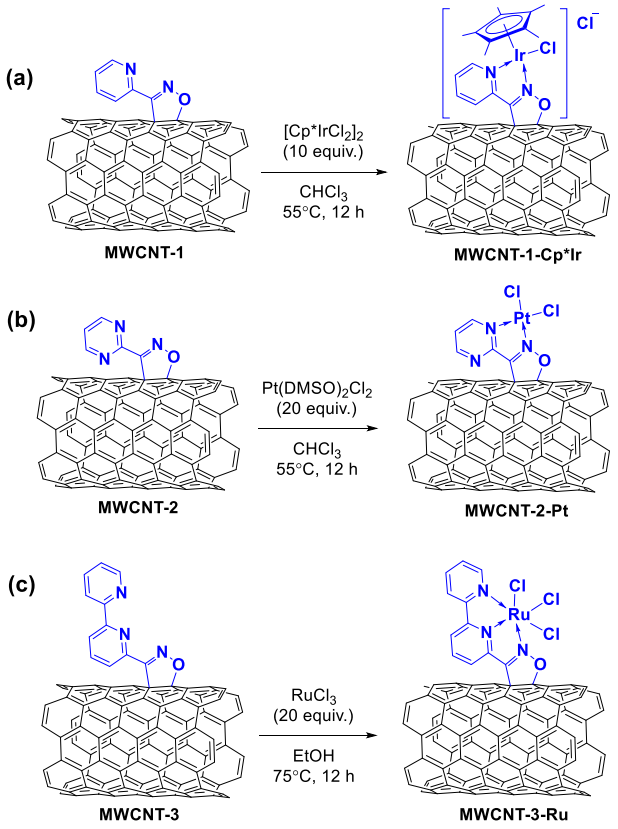

[a]The amounts of metal precursors are relative to the amount of functional groups determined by XPS. MWCNTs are simplified as SWCNTs in the illustration for clarity.

Table 2. Elemental Composition of Metal-Chelated MWCNTs

	XPS composition (atom %)				
sample	C 1s	N 1s	O 1s	Cl 2p	metal
MWCNT-1-Cp*Ir	76.3	6.8	6.9	7.5	2.5 (Ir 4f)
MWCNT-2-Pt	68.2	14.4	9.4	5.0	3.0 (Pt 4f)
MWCNT-3-Ru	87.5	4.2	5.2	2.2	0.9 (Ru 3p)
FLG-1-Cp*Ir	72.6	9.2	6.7	8.5	3.0 (Ir 4f)
MWCNT-1-Ni	83.4	6.4	5.4	2.8	2.0 (Ni 2p)

that has high mass resolution for the acquisition of molecular information from the surface of a material.[73] The MWCNT surfaces are bombarded with Bi_3^+, and the secondary ions are evaluated by mass spectrometry in the context of fragments originating from the surface functional groups. As shown in Figure 4, significantly more signals, which are attributed to unsaturated hydrocarbon fragments, are observed in the functionalized MWCNTs in comparison to the pristine unfunctionalized material. In particular, unambiguous peaks at m/z 78, 79, and 155 are indicative of the pyridyl, pyrimidyl, and bipyridyl fragments, respectively. These specific fragments are attributed to the different isoxazole groups that had been covalently fused to the MWCNTs. Prominent C_nN^- peaks, which originate from the nitrogen-containing functional groups,[74] are observed in the functionalized MWCNTs in negative mode (Figure S12). The collective evidence from Raman, XPS, and ToF-SIMS analyses supports that MWCNTs

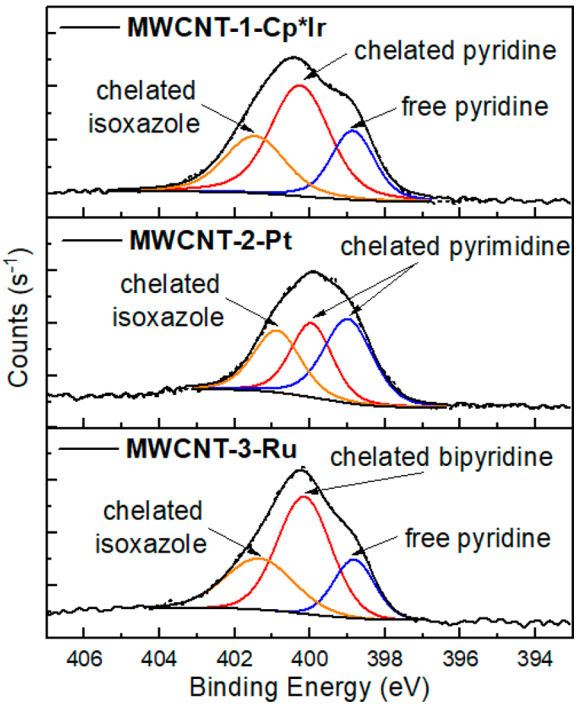

Figure 6. XPS N 1s spectra of **MWCNT-1-Cp*Ir** (top), **MWCNT-2-Pt** (middle), and **MWCNT-3-Ru** (bottom).

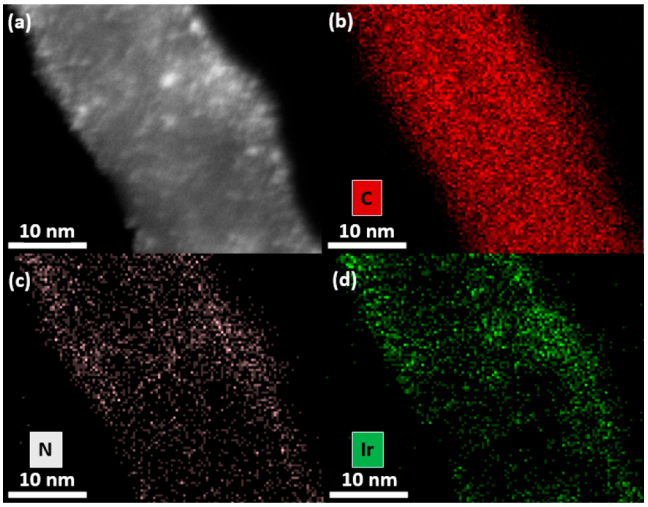

Figure 7. (a) HAADF-STEM image of **MWCNT-1-Cp*Ir**. (b–d) STEM-EDS elemental mapping of **MWCNT-1-Cp*Ir**.

have been successfully covalently functionalized by cycloaddition of nitrile oxides to give the structures shown in Scheme 1.

We have been interested to see if our methods could be generalized to functionalize other carbon nanomaterials, including few-layer graphene. As shown in Scheme 2, few-layered graphene (**p-FLG**) nanoplatelets were subjected to the microwave conditions and *in situ* generation of 2-pyridyl nitrile oxide to yield the isoxazoline-functionalized product **FLG-1**. Successful covalent modification of the graphene layers was confirmed by the significant increase in D/G band ratio in the Raman spectra (Figure S13). The average number of layers of the material was found to have increased slightly, as indicated by the diminished 2D/G band ratio,[75] wherein the aggregation may be promoted by microwave heating. A remarkably high

https://doi.org/10.1021/jacs.1c05439
J. Am. Chem. Soc. 2021, 143, 10441−10453

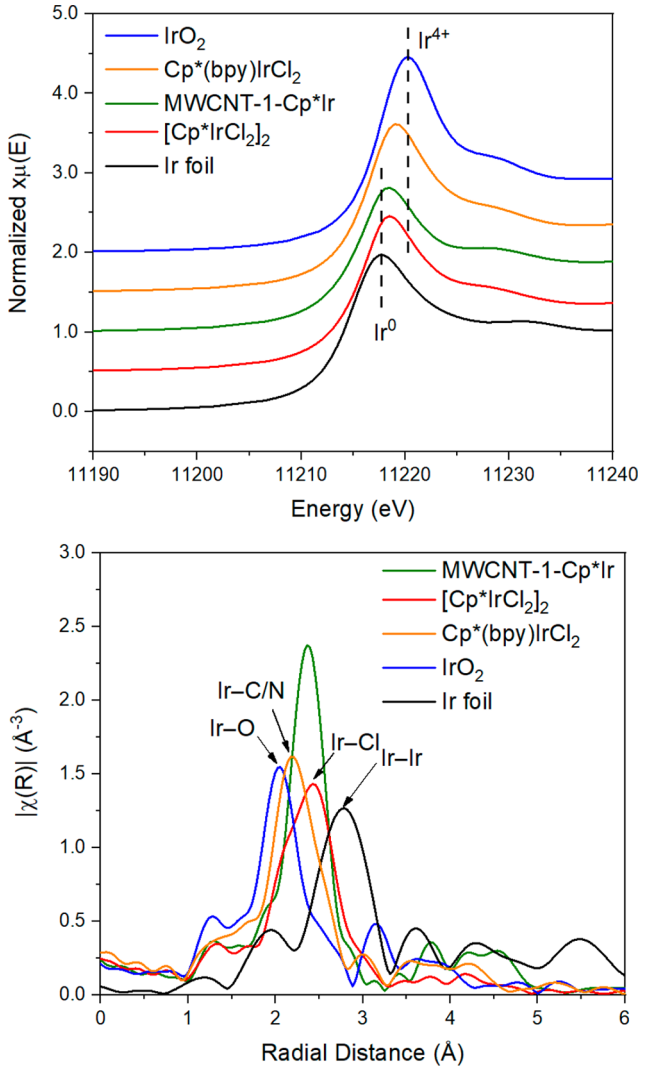

Figure 8. XANES data (top) and Fourier-transformed EXAFS spectra (bottom) at the Ir L_3-edge of **MWCNT-1-Cp*Ir**, $[Cp^*IrCl_2]_2$, $Cp^*(bpy)IrCl_2$, IrO_2, and Ir foil.

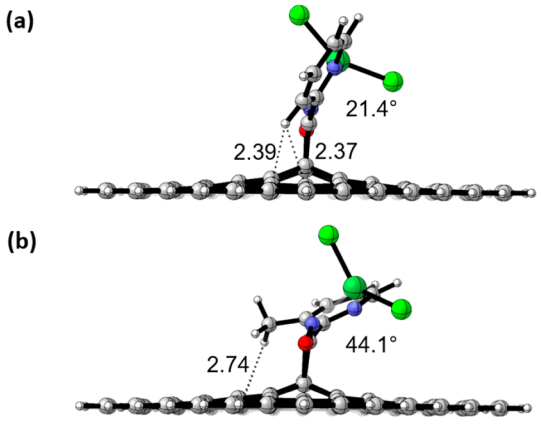

Figure 9. Optimized structures of (a) **G-1-Ni_frozen** and (b) **G-4-Ni_frozen** fragments. All distances are shown in Å.

degree of functionalization of 7.7 functional groups per 100 graphene carbon atoms in **FLG-1** was determined by XPS (Figure S14). Notably, this material is among the most densely functionalized graphenes reported to date (Table S3). This result is particularly exciting because it is challenging to covalently functionalize graphene layers as a result of the lack of a basal plane curvature.[76,77] A high-resolution XPS spectrum of the N 1s region confirmed the identity of the 2-pyridylisoxazole functional group by the characteristic pyridine and isoxazole N 1s peaks with the expected stoichiometry (Figure S15). The high functionalization efficiency is likely facilitated by the high dispersibility of **p-FLG** in *o*DCB as a result of its smaller domain size. As shown in Figure 5, at a concentration of 0.1 mg/mL, **FLG-1** is easily dispersed in water with mild bath sonication. This solution is stable for weeks, whereas pristine **p-FLG** has insignificant dispersibility in water. The stark increase in hydrophilicity of **FLG-1** represents a clear macroscopic manifestation of its highly functionalized nature.

We have explored the metal-binding properties of isoxazoline-functionalized MWCNTs and FLG (Scheme 3) with $[Cp^*IrCl_2]_2$ ($Cp^* = \eta^5$-C_5Me_5), *cis*-$Pt(DMSO)_2Cl_2$ (DMSO = dimethyl sulfoxide), and $RuCl_3$ hydrate. The selected metal species are well-known to complex pyridinic nitrogens. The isoxazoline-functionalized MWCNTs were dispersed in chloroform or ethanol by bath sonication, mixed with the metal complex precursors, and then heated for 12 h before collection by filtration. After extensive washing with ethanol, *N*,*N*-dimethylformamide, and acetone to remove the unbound metal species, the resulting materials were evaluated with XPS (Figures S17–S19). As summarized in Table 2, all of the added metallic elements were observed by XPS. In particular, **MWCNT-1-Cp*Ir** displayed a 2.5 atom % or 26 wt % Ir(III), **MWCNT-2-Pt** was found to contain 3.0 atom % or 30 wt % Pt(II), and **MWCNT-3-Ru** was found to contain 0.9 atom % or 7 wt % Ru(III). The immobilized metal species were also found to have binding energies by XPS mostly identical with those of their homogeneous precursors, suggesting the unperturbed oxidation state of the metal species (Figures S20–S22). This observation is in stark contrast with the previous reports of spontaneous reduction of Ru(III) and Pt(II) compounds by pristine CNTs,[78,79] thereby showcasing the stabilizing effect resulting from the surface chelating groups. **FLG-1** has also shown good metal-binding ability by incorporating 3.0 atom % or 29 wt % of Ir(III) (Figure S23). Moreover, beyond the scope of precious metals, earth-abundant Ni(II) can also be effectively chelated to **MWCNT-1** (Scheme S1 and Figures S24 and S25). All evidence suggests that our platform has general utility for the formation of metal–carbon nanomaterial complexes.

To test the hypothesis that metal binding occurred via metal chelation rather than simple physisorption, we evaluated the high-resolution XPS spectra of the N 1s regions of the metal–MWCNT composite materials (Figure 6). In comparison to the spectra of the starting materials in Figure 3, we find that the characteristic pyridinic peaks at 398.6 eV have decreased significantly whereas new peaks have emerged at around 400.3 and 401.5 eV. These peaks correspond to the chelated pyridinic N 1s peaks and chelated isoxazole N 1s peaks, respectively, which as expected have slightly higher binding energy in comparison to their nonchelated counterparts.[80,81] We further measured the XPS N 1s spectrum of $[(ppy)_2IrCl]_2$ (ppy = 2-phenylpyridine) as an external reference to confirm the binding energy of the chelated pyridinic nitrogen (Figure S26).

It was important to further demonstrate that the metal species chelated on the carbon nanomaterials are molecularly

https://doi.org/10.1021/jacs.1c05439
J. Am. Chem. Soc. 2021, 143, 10441–10453

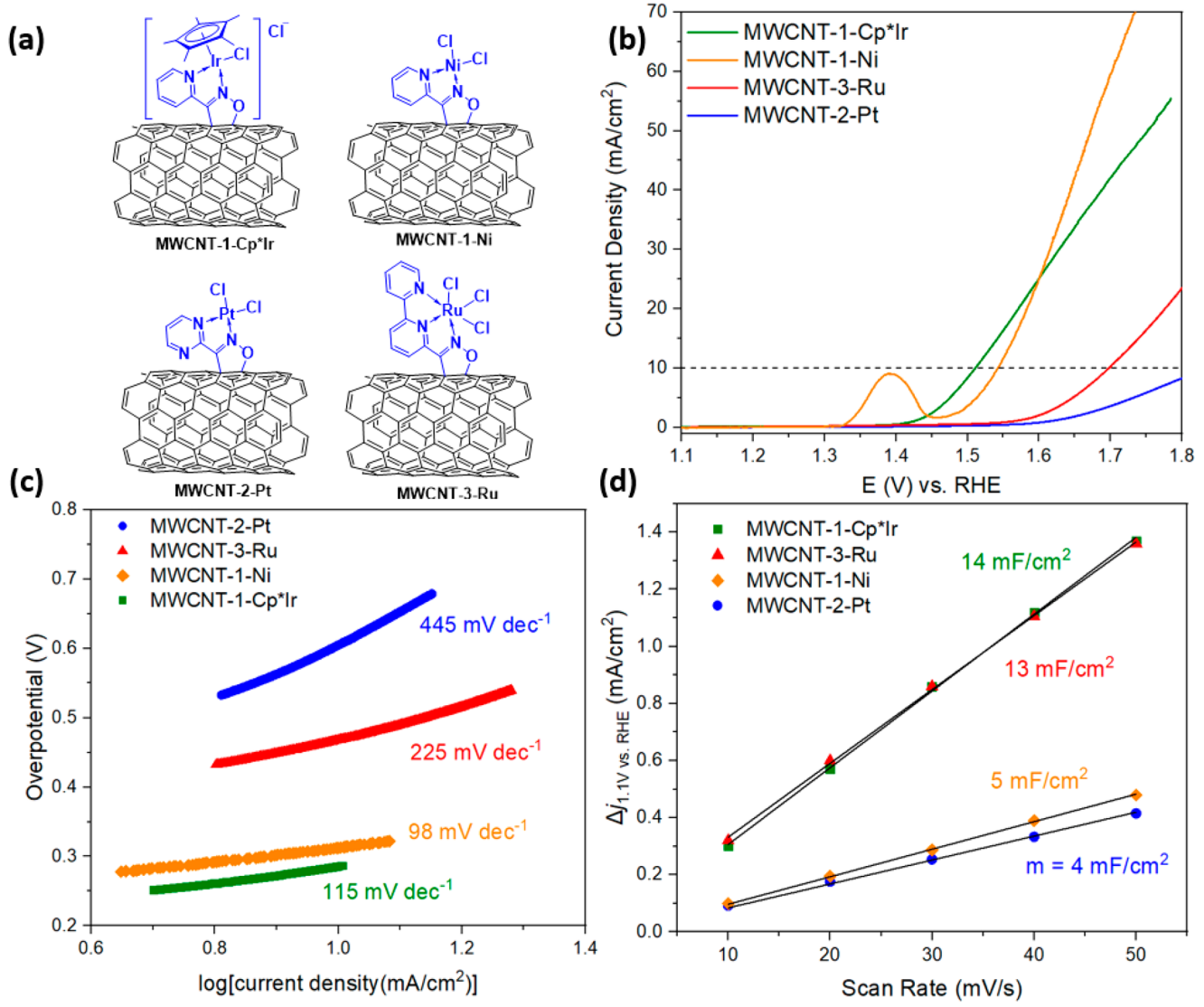

Figure 10. (a) Structures of metal-functionalized MWCNTs. MWCNTs are simplified as SWCNTs in the illustration for clarity. (b) LSV curves of **MWCNT-1-Cp*Ir** (green), **MWCNT-1-Ni** (orange), **MWCNT-2-Pt** (blue), and **MWCNT-3-Ru** (red) for the OER in 1 M KOH. (c) Tafel plots of different catalysts for the OER in 1 M KOH. (d) Estimation of double-layer capacitance C_{dl} by fitting the current-density variation at 1.1 V vs RHE against the scan rate.

dispersed as opposed to aggregating into nanoparticles/clusters. In this context **MWCNT-1-Cp*Ir**, as a representative composition, was imaged using a scanning transmission electron microscope (STEM) and the map of the respective elements was revealed by energy dispersive spectroscopy (EDS). As shown in Figure 7, nitrogen and iridium species are found to be uniformly dispersed on MWCNT and their locations seem to correlate with each other. **MWCNT-1-Cp*Ir** has also been analyzed by STEM-EDS at multiple locations and lower magnification to ensure that the dispersive nature of the iridium species is consistent throughout the material (Figure S28). X-ray absorption spectroscopy (XAS) studies were also performed to support our claim that the chelated metal species are molecularly dispersed on the modified carbon nanomaterials. In the extended X-ray absorption fine structure (EXAFS) analysis (Figure 8), **MWCNT-1-Cp*Ir** is shown to have a local coordination structure distinct from those of the reference Ir foil and IrO_2, indicating the absence of Ir−Ir bonds and IrO_2 clusters in the material. A broad scattering peak is observed for **MWCNT-1-Cp*Ir** that covers a range of distance from 2.0 to 2.5 Å and can be attributed to the existence of Ir−C, Ir−N, and Ir−Cl bonds, comparable with those of the reference compounds $[Cp^*IrCl_2]_2$ and Cp*-(bpy)$IrCl_2$ (bpy = 2,2′-bipyridine). Moreover, consistent with the XPS results, the X-ray absorption near-edge structure (XANES) at the Ir L_3-edge (Figure 8) shows that the white line peak position of **MWCNT-1-Cp*Ir** is very similar to that of $[Cp^*IrCl_2]_2$, suggesting the unperturbed oxidation state of Ir(III) after the metal chelation process. Similarly, the molecular dispersed nature of other metal-functionalized carbon nanomaterials such as **MWCNT-1-Ni** is also evidenced by XAS results (Figure S29).

To further understand the metal chelating ability of the isoxazoline−nanocarbon materials, we employed computational tools to investigate the thermodynamics of the metal chelation events on the graphene surface. In a representative system, **MWCNT-1-Ni** has been modeled as **G-1-Ni** on a finite-size polybenzenoid (36 fused benzene rings) hydrocarbon and the energetics of the ligand substitution process has been studied. An unrestricted DFT method was used, as

https://doi.org/10.1021/jacs.1c05439
J. Am. Chem. Soc. 2021, 143, 10441−10453

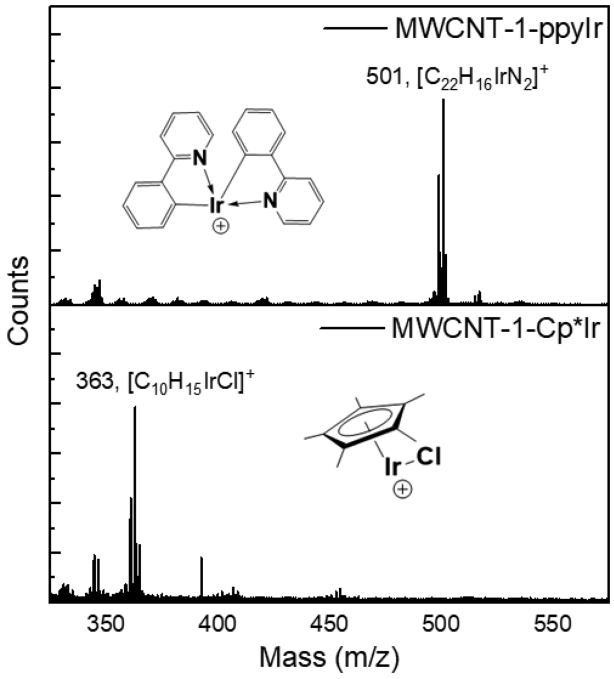

Figure 11. ToF-SIMS spectra of **MWCNT-1-ppyIr** (top) and **MWCNT-1-Cp*Ir** (bottom) in positive mode, showing fragments from their respective molecular precursors.

radical character has been reported in polyacenes and graphene fragments.[82−85,53] Energy calculations suggest that the ground-state Ni(II)-containing species are likely to be high spin (Table S4). The formation of **G-1-Ni** is found to be exothermic with a ΔG value of −3.3 kcal/mol (Figure S43). A slight curvature has been observed in the optimized graphene structures due to the edge effect. To give a more realistic representation of the graphene plane, an additional limit has been imposed on the structures where the optimization was performed with the outermost carbon atoms frozen in a planar geometry. The optimized structure of **G-1-Ni_frozen** is shown in Figure 9a, where a dihedral angle of 21.4° is observed between the pyridine and the isoxazole rings. The ΔG value of chelation in this case (ΔG_frozen) was found to be slightly higher (−2.0 kcal/mol) yet still thermodynamically favorable. For reference, metal chelation of the small-molecule analogue **Py-Iso** has also been evaluated (Figure S44). A simple distortion-interaction analysis shows a reasonable distortion energy of 9.3 kcal/mol (**G-1_frozen** → **G-1_distort_frozen**) for the pyridine ring to rotate and move into the position for metal chelation. As shown in Figure 9a and Figure S47, the H on the 3-position of the pyridine ring is in close contact with the graphene plane. Therefore, we were interested in probing the substituent steric effect on metal chelation. To this end, an additional methyl group has been introduced to the 3-position of the pyridine ring (**MWCNT-4**, Figure S30) to increase the steric bulk. Attempts to synthesize **MWCNT-4-Ni** (Scheme S2) were unsuccessful with only trace Ni(II) incorporation (Figure S31 and Table S1). This experimental observation is in good agreement with computational results, where the formation of **G-4-Ni_frozen** was found to be unfavorable (Figure S45). The optimized structure of **G-4-Ni_frozen** (Figure 9b) shows a highly distorted chelate structure with a large dihedral angle of 44.1° between the pyridine and the isoxazole rings. The $\Delta\Delta G$ value of chelation between the H-substituted and methyl-substituted isoxazoline graphene was found to be 8.3 kcal/mol, suggesting a 6 orders of magnitude difference in equilibrium constants. These results highlight the structure−activity relationship between the steric bulk of the pyridyl-isoxazoline moieties on graphene and their ability to chelate metal species.

This dense functionalization of carbon nanomaterials with transition metals represents a new platform for heterogeneous catalysis. The structure of the isoxazoline ligands with a π-electronic system proximate to the graphene facilitates electronic coupling. The conducting properties of the carbon nanomaterials and molecularly dispersed nature of the metal species were expected to provide highly active electrocatalysts or precatalysts. As a proof of concept, the catalytic performance in the oxygen evolution reaction (OER) has been evaluated by linear sweep voltammetry (LSV) and a Tafel slope analysis. The electrochemically active surface area (ECSA) has also been characterized by estimating the double-layer capacitance (C_{dl}). The functionalized MWCNTs were dispersed in ethanol, mixed with a 5 wt % Nafion solution, and subsequently drop-casted on a carbon paper electrode to fabricate the working electrode for the OER process in 1 M KOH electrolyte. As shown by its LSV curve in Figure 10b, **MWCNT-1-Cp*Ir** exhibits excellent OER activity with an overpotential of 280 mV at 10 mA/cm^2, which places it among the best-performing CNT-based OER catalysts reported.[86−95] The molecular analogues of **MWCNT-1-Cp*Ir** have been extensively studied as water oxidation catalysts.[96−101] For reference the commercial carbon paper electrode, **p-MWCNT**, and **MWCNT-1** were found to possess poor OER activity with overpotentials of greater than 600 mV (Figure S32). Notably, **MWCNT-1-Cp*Ir** outperformed the mixture of pristine MWCNTs and commercial IrO_2 with the same metal loading (**IrO_2/p-MWCNT**, 25 wt % Ir) in terms of overpotentials, current densities, and kinetics in the OER catalysis (Figures S32 and S33). This feature confirms that the covalent functionalization of metal chelators on MWCNTs to integrate transition-metal complexes produces more efficient catalysts. In contrast, even though the Ir(III) content is higher in **FLG-1-Cp*Ir**, its OER activity was found to be less than ideal (Figure S32), possibly due to poor contact between the material and the electrode and/or the lower conductance of the highly functionalized FLG.

The OER performances of several other transition-metal−MWCNT complexes were evaluated (Figure 10). **MWCNT-3-Ru** showed moderate OER activity with an overpotential of 460 mV, whereas **MWCNT-2-Pt** was found to be OER inactive. The inferior OER performance of the high-metal-content **MWCNT-2-Pt** was unexpected and may be attributed to a ligand effect and/or the lower conductance as a result of the high degree of functionalization. **MWCNT-3-Ru** has a significantly lower metal content than **MWCNT-1-Cp*Ir** as a result of the lower degree of functionalization in **MWCNT-3**. However, **MWCNT-1-Ni**, which contains earth-abundant Ni(II), was found to not only possess excellent OER activity similar to that of **MWCNT-1-Cp*Ir** with an overpotential of 310 mV but also faster OER kinetics as illustrated by a Tafel analysis (Figure 10c). Moreover, the current density of **MWCNT-1-Ni** reaches 69 mA/cm^2 at an overpotential of 500 mV, which is more than 2 times higher than that of the **IrO_2/p-MWCNT** mixture (25 wt % Ir) at the same overpotential (33 mA/cm^2). This is particularly exciting, as nickel represents a low-cost substitute for precious-metal oxides that are widely used as OER catalysts industrially.[102,103]

https://doi.org/10.1021/jacs.1c05439
J. Am. Chem. Soc. 2021, 143, 10441−10453

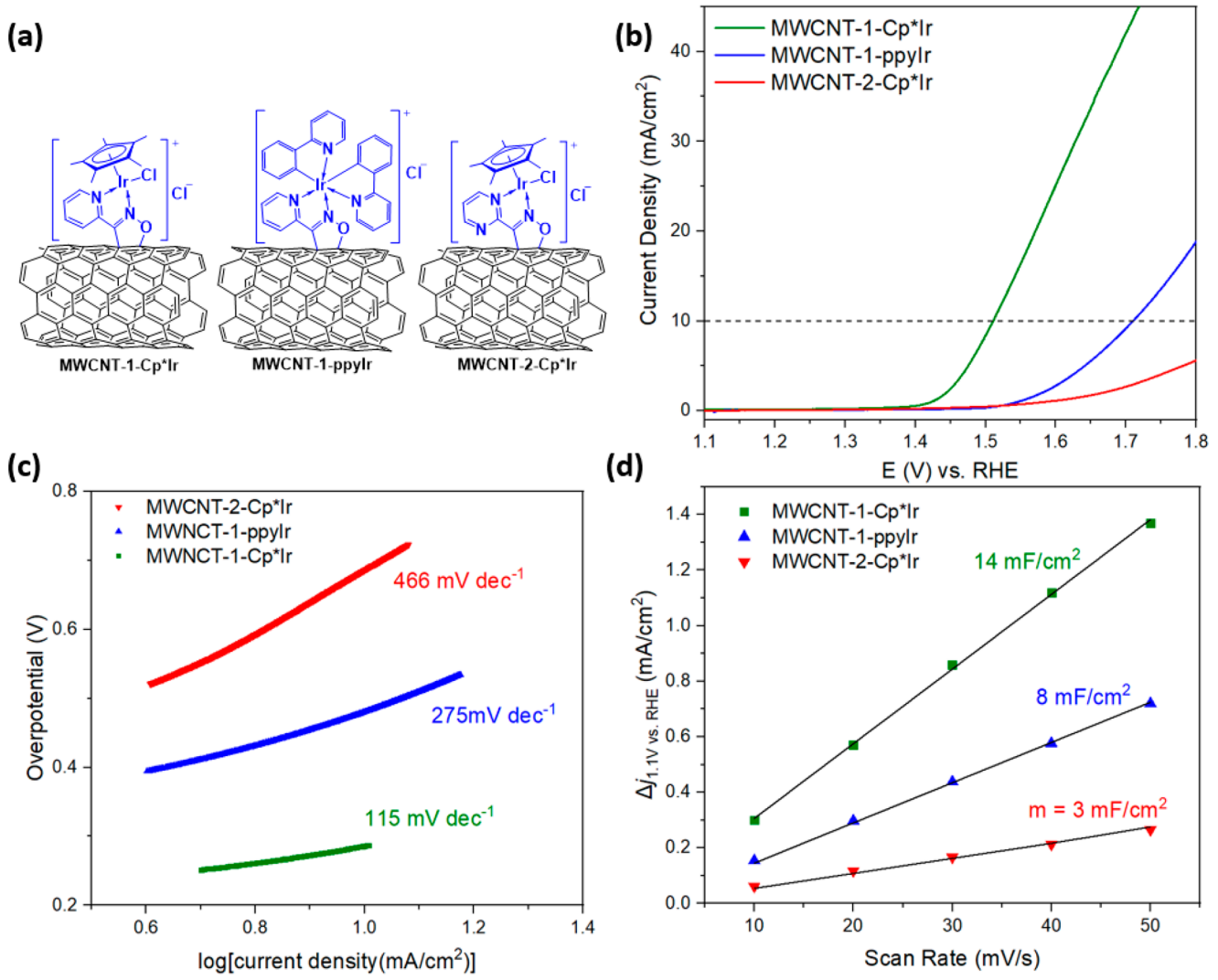

Figure 12. (a) Structures of metal-functionalized MWCNTs. MWCNTs are simplified as SWCNTs in the illustration for clarity. (b) LSV curves of **MWCNT-1-Cp*Ir** (green), **MWCNT-1-ppyIr** (blue), and **MWCNT-2-Cp*Ir** (blue) for the OER in 1 M KOH. (c) Tafel plots of different catalysts for the OER in 1 M KOH. (d) Estimation of double-layer capacitance C_{dl} by fitting the current-density variation at 1.1 V vs RHE against the scan rate.

The long-term stability of **MWCNT-1-Ni** was also evaluated by chronopotentiometry (CP) at a current density of 10 mA/cm^2, and no significant loss of OER activity was observed after 16 h of operation (Figure S35). XPS analysis of **MWCNT-1-Ni** after CP shows a near-complete loss of chlorine content and slight changes in Ni 2p peaks (Figures S36 and S37), suggesting the speciation of nickel chlorides to nickel hydroxides/oxyhydroxides during the OER process. To further characterize the catalytically active metal species, EXAFS analysis of **MWCNT-1-Ni** after the OER shows a Ni local coordination environment that closely resembles that of $Ni(OH)_2$ (Figure S38). Notably, a prominent oxidation peak is observed at around 1.4 V for **MWCNT-1-Ni**, which corresponds to the Ni(II)/Ni(III) oxidation event.[104−106] XANES results at the Ni K-edge (Figure S38) also reveal that the white-line position of **MWCNT-1-Ni** shifted to a higher energy after the OER, suggesting an increase in oxidation state for the Ni center, further supporting the formation of nickel oxyhydroxides during the OER. Moreover, on comparison of the total charge transfer in this oxidation event to the amount of Ni(II) drop-casted on the carbon paper electrode, we found that about 88% of the deposited Ni(II) is accounted for in this oxidation (Figure S39), thereby underscoring the efficient electrochemical coupling between the metal center and MWCNTs.

Our complexation strategy provides molecular level structural control of the heterogeneous catalyst, and as such the catalytic activity can be modulated by the surrounding ligand structures. To probe this aspect, we have synthesized a series of Ir(III)−MWCNT complexes bearing different ligands, as shown in Figure 12a. **MWCNT-1-ppyIr** is synthesized via ligand substitution from the $[(ppy)_2IrCl]_2$ precursor, and **MWCNT-2-Cp*Ir** is derived from **MWCNT-2** and $[Cp^*IrCl_2]_2$ (Scheme S3). Their chemical compositions have been characterized by XPS, which reveals levels of Ir(III) content comparable with those of **MWCNT-1-Cp*Ir** (Figures S40 and S41 and Table S2). Tof-SIMS was particularly useful in unambiguously assigning and distinguishing the ligand structures present on these Ir(III)-MWCNT complexes. As shown in Figure 11, $[ppy_2Ir]^+$ and $[Cp^*IrCl]^+$ ions were the dominant ions, supporting the proposed structures of **MWCNT-1-ppyIr** and **MWCNT-1-Cp*Ir**, respectively.

https://doi.org/10.1021/jacs.1c05439
J. Am. Chem. Soc. 2021, 143, 10441−10453

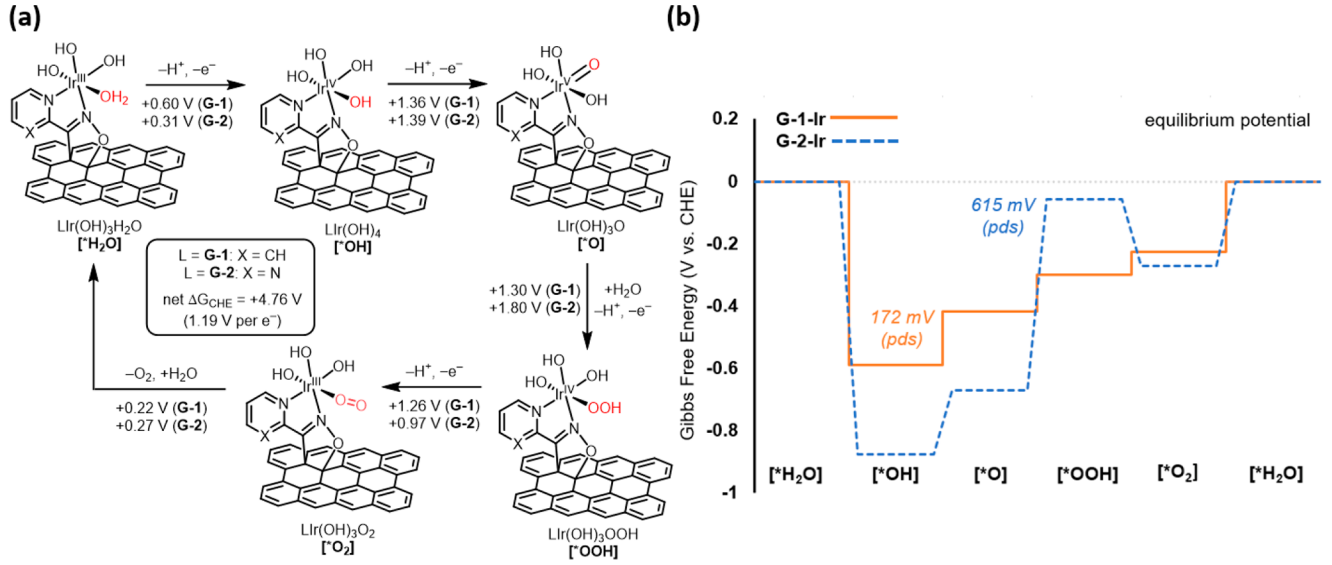

Figure 13. (a) Proposed OER pathway and computed energies for **G-1-Ir** and **G-2-Ir** modeled on a (6 × 6) graphene fragment. The graphene model in the illustration is truncated for clarity. (b) OER energy profile diagrams at the equilibrium potential (+1.19 V vs CHE) for **G-1-Ir** (orange, solid line) and **G-2-Ir** (blue, dashed line). The potential-determining steps (pds) of the OER are indicated.

The OER performances of **MWCNT-1-ppyIr** and **MWCNT-2-Cp*Ir** are compared with that of **MWCNT-1-Cp*Ir** in Figure 12. Interestingly, both variants of **MWCNT-1-Cp*Ir** were found to be less active in the OER. The overpotentials of **MWCNT-1-ppyIr** and **MWCNT-2-Cp*Ir** were determined to be 480 and 690 mV, respectively. The OER kinetics and ESCA were also found to follow the same trend, **MWCNT-1-Cp*Ir** > **MWCNT-1-ppyIr** > **MWCNT-2-Cp*Ir**, despite having similar Ir(III) contents. The difference in their OER activity seems to correlate with the catalytic activity of their molecular analogues for water oxidation. For the cyclometalated **MWCNT-1-ppyIr**, its molecular analogue was reported to be inactive in water oxidation due to the lack of an accessible coordination site.[107] On the other hand, the Cp*–Ir(III) water oxidation catalysts bearing weaker donor pyrimidyl ligands display lower catalytic activity in comparison to their pyridyl counterparts.[97,101] To evaluate whether this reasoning in the context of molecular catalysts applies analogously to heterogeneous surface-bound catalysts, we have also performed computational studies to probe the ligand effect (pyridyl vs pyrimidyl) on OER activity. In our studies, **MWCNT-1-Cp*Ir** and **MWCNT-2-Cp*Ir** were represented by simplified models each supported by a 6 × 6 slab of graphene: **G-1-Ir** and **G-2-Ir**, respectively. The free energy profile of the OER reaction was calculated by following the well-established four-electron water nucleophilic attack (WNA) mechanism.[97,99,101,108−112] The most stable structures of key intermediates and their computed energies are summarized in Figure 13a. At an external potential that renders the overall process thermoneutral (+1.19 V relative to the computational hydrogen electrode (CHE)), the potential-determining steps (pds) have been identified in the OER pathways for **G-1-Ir** and **G-2-Ir** (Figure 13b). For the electron-deficient **G-2-Ir**, both formation of the oxo and subsequent attack by water were found to be significantly less favorable than for the pyridine-based **G-1-Ir**. The difference in theoretical overpotentials was found to be 443 mV, which is consistent with the 410 mV difference observed experimentally. Moreover, the change in pds could significantly affect the OER kinetics, as demonstrated by the drastically different Tafel slopes observed between **MWCNT-1-Cp*Ir** and **MWCNT-2-Cp*Ir** (Figure 12c). Although other factors could plausibly contribute to the difference in catalytic efficiency, these results suggest that the ligand electronic effect could be a considerable influence. More importantly, the present results demonstrate that we can tune the catalytic activities of heterogeneous molecular catalysts to a significant extent through rational ligand design. As a result, our strategy of metal complexation on carbon nanomaterials holds great potential in creating new avenues for catalyst discovery for many other significant processes.

CONCLUSION

We have synthesized a new class of metal chelating carbon nanomaterials and demonstrated their utility in transition-metal-based electrocatalysis. Isoxazoline surface functionalization is efficient and was found to create covalent ligands that give consistent results indicative of the expected molecular structures. The electroactivity is also consistent with the structures that were designed to produce effective electronic coupling between the chelated metal complexes and the carbon nanomaterial support. We probed the electrocatalytic activity of these modified materials with applications in the oxygen evolution reaction. The results described herein suggest that this approach to create functionalized nanomaterials has great promise for new designer heterogeneous catalytic systems.

ASSOCIATED CONTENT

Supporting Information

The Supporting Information is available free of charge at https://pubs.acs.org/doi/10.1021/jacs.1c05439.

Instrumentation and materials, experimental details, additional characterization data, additional electrochemical test results, optimized Cartesian coordinates and energies, and NMR spectra of new compounds (PDF)

https://doi.org/10.1021/jacs.1c05439
J. Am. Chem. Soc. 2021, 143, 10441−10453

AUTHOR INFORMATION

Corresponding Author

Timothy M. Swager − *Department of Chemistry and Institute for Soldier Nanotechnologies, Massachusetts Institute of Technology, Cambridge, Massachusetts 02139, United States;* orcid.org/0000-0002-3577-0510; Email: tswager@mit.edu

Authors

Shao-Xiong Lennon Luo − *Department of Chemistry and Institute for Soldier Nanotechnologies, Massachusetts Institute of Technology, Cambridge, Massachusetts 02139, United States;* orcid.org/0000-0001-5308-4576

Richard Y. Liu − *Department of Chemistry and Institute for Soldier Nanotechnologies, Massachusetts Institute of Technology, Cambridge, Massachusetts 02139, United States;* orcid.org/0000-0003-0951-6487

Sungsik Lee − *X-ray Science Division, Advanced Photon Source, Argonne National Laboratory, Lemont, Illinois 60439, United States;* orcid.org/0000-0002-1425-9852

Complete contact information is available at: https://pubs.acs.org/10.1021/jacs.1c05439

Notes

The authors declare no competing financial interest.

ACKNOWLEDGMENTS

This work was supported by the National Institute of Environmental Health Sciences Superfund Basic Research Program, National Institutes of Health, P42 ES027707, the National Science Foundation DMR-1809740, and KAUST sensor project REP-2719. This work was performed in part at the Center for Nanoscale Systems (CNS), a member of the National Nanotechnology Coordinated Infrastructure Network (NNCI), which is supported by the National Science Foundation under NSF award no. ECCS-2025158. CNS is part of Harvard University. This work was performed in part at the Analytical Instrumentation Facility (AIF) at North Carolina State University, which is supported by the State of North Carolina and the National Science Foundation (award number ECCS-2025064). The AIF is a member of the North Carolina Research Triangle Nanotechnology Network (RTNN), a site in the National Nanotechnology Coordinated Infrastructure (NNCI). We thank Dr. Jules Gardener for assistance with STEM imaging and Dr. Chuanzhen Zhou for assistance with ToF-SIMS experiments. We are grateful for computational resources provided by the Massachusetts Green High-Performance Computing Center (MGHPCC) C3DDB cluster. This research used resources of the Advanced Photon Source, a U.S. Department of Energy (DOE) Office of Science User Facility, operated for the DOE Office of Science by Argonne National Laboratory under Contract No. DE-AC02-06CH11357. We thank Prof. Máté Bezek, Prof. Tien-Lin Wu, Dr. Darryl Fong, Dr. Ru-Qiang Lu, Haosheng Feng, and Prof. Maggie He for suggestions and insightful discussions.

REFERENCES

(1) Iijima, S. Helical Microtubules of Graphitic Carbon. *Nature* **1991**, *354*, 56−58.

(2) Falvo, M. R.; Clary, G. J.; Taylor, R. M.; Chi, V.; Brooks, F. P.; Washburn, S.; Superfine, R. Bending and Buckling of Carbon Nanotubes under Large Strain. *Nature* **1997**, *389*, 582−584.

(3) Saito, R.; Fujita, M.; Dresselhaus, G.; Dresselhaus, M. S. Electronic Structure of Graphene Tubules Based on C_{60}. *Phys. Rev. B: Condens. Matter Mater. Phys.* **1992**, *46*, 1804−1811.

(4) Hamada, N.; Sawada, S.-i.; Oshiyama, A. New One-Dimensional Conductors: Graphitic Microtubules. *Phys. Rev. Lett.* **1992**, *68*, 1579−1581.

(5) Pop, E.; Mann, D.; Wang, Q.; Goodson, K.; Dai, H. Thermal Conductance of an Individual Single-Wall Carbon Nanotube above Room Temperature. *Nano Lett.* **2006**, *6*, 96−100.

(6) Dresselhaus, M. S.; Dresselhaus, G.; Charlier, J. C.; Hernandez, E. Electronic, Thermal and Mechanical Properties of Carbon Nanotubes. *Philos. Trans. R. Soc., A* **2004**, *362*, 2065−2098.

(7) Novoselov, K. S.; Geim, A. K.; Morozov, S. V.; Jiang, D.; Zhang, Y.; Dubonos, S. V.; Grigorieva, I. V.; Firsov, A. A. Electric Field Effect in Atomically Thin Carbon Films. *Science* **2004**, *306*, 666−669.

(8) Geim, A. K.; Novoselov, K. S. The rise of graphene. *Nat. Mater.* **2007**, *6*, 183−191.

(9) Yang, Z.; Ren, J.; Zhang, Z.; Chen, X.; Guan, G.; Qiu, L.; Zhang, Y.; Peng, H. Recent Advancement of Nanostructured Carbon for Energy Applications. *Chem. Rev.* **2015**, *115*, 5159−5223.

(10) Sun, H.; Zhang, Y.; Zhang, J.; Sun, X.; Peng, H. Energy harvesting and storage in 1D devices. *Nat. Rev. Mater.* **2017**, *2*, 17023.

(11) Chen, X.; Paul, R.; Dai, L. Carbon-based supercapacitors for efficient energy storage. *Natl. Sci. Rev.* **2017**, *4*, 453−489.

(12) Du, J.; Pei, S.; Ma, L.; Cheng, H.-M. 25th Anniversary Article: Carbon Nanotube- and Graphene-Based Transparent Conductive Films for Optoelectronic Devices. *Adv. Mater.* **2014**, *26*, 1958−1991.

(13) Hu, C.; Qu, J.; Xiao, Y.; Zhao, S.; Chen, H.; Dai, L. Carbon Nanomaterials for Energy and Biorelated Catalysis: Recent Advances and Looking Forward. *ACS Cent. Sci.* **2019**, *5*, 389−408.

(14) Zhu, C.; Li, H.; Fu, S.; Du, D.; Lin, Y. Highly Efficient Nonprecious Metal Catalysts towards Oxygen Reduction Reaction Based on Three-Dimensional Porous Carbon Nanostructures. *Chem. Soc. Rev.* **2016**, *45*, 517−531.

(15) Liu, X.; Dai, L. Carbon-Based Metal-Free Catalysts. *Nat. Rev. Mater.* **2016**, *1*, 16064.

(16) Navalon, S.; Dhakshinamoorthy, A.; Alvaro, M.; Garcia, H. Carbocatalysis by Graphene-Based Materials. *Chem. Rev.* **2014**, *114*, 6179−6212.

(17) Schroeder, V.; Savagatrup, S.; He, M.; Lin, S.; Swager, T. M. Carbon Nanotube Chemical Sensors. *Chem. Rev.* **2019**, *119*, 599−663.

(18) Wang, J. Carbon-Nanotube Based Electrochemical Biosensors: A Review. *Electroanalysis* **2005**, *17*, 7−14.

(19) Kauffman, D. R.; Star, A. Carbon Nanotube Gas and Vapor Sensors. *Angew. Chem., Int. Ed.* **2008**, *47*, 6550−6570.

(20) Meyyappan, M. Carbon Nanotube-Based Chemical Sensors. *Small* **2016**, *12*, 2118−2129.

(21) Kruss, S.; Hilmer, A. J.; Zhang, J.; Reuel, N. F.; Mu, B.; Strano, M. S. Carbon Nanotubes as Optical Biomedical Sensors. *Adv. Drug Delivery Rev.* **2013**, *65*, 1933−1950.

(22) Shao, Y.; Wang, J.; Wu, H.; Liu, J.; Aksay, I. A.; Lin, Y. Graphene Based Electrochemical Sensors and Biosensors: A Review. *Electroanalysis* **2010**, *22*, 1027−1036.

(23) Varghese, S. S.; Lonkar, S.; Singh, K. K.; Swaminathan, S.; Abdala, A. Recent Advances in Graphene Based Gas Sensors. *Sens. Actuators, B* **2015**, *218*, 160−183.

(24) Hong, G.; Diao, S.; Antaris, A. L.; Dai, H. Carbon Nanomaterials for Biological Imaging and Nanomedicinal Therapy. *Chem. Rev.* **2015**, *115*, 10816−10906.

(25) Baptista, F. R.; Belhout, S. A.; Giordani, S.; Quinn, S. J. Recent Developments in Carbon Nanomaterial Sensors. *Chem. Soc. Rev.* **2015**, *44*, 4433−4453.

(26) Panwar, N.; Soehartono, A. M.; Chan, K. K.; Zeng, S.; Xu, G.; Qu, J.; Coquet, P.; Yong, K.-T.; Chen, X. Nanocarbons for Biology and Medicine: Sensing, Imaging, and Drug Delivery. *Chem. Rev.* **2019**, *119*, 9559−9656.

(27) Wang, H.; Chen, Q.; Zhou, S. Carbon-Based Hybrid Nanogels: A Synergistic Nanoplatform for Combined Biosensing, Bioimaging, and Responsive Drug Delivery. *Chem. Soc. Rev.* **2018**, *47*, 4198−4232.
(28) Kumar, S.; Rani, R.; Dilbaghi, N.; Tankeshwar, K.; Kim, K.-H. Carbon Nanotubes: A Novel Material for Multifaceted Applications in Human Healthcare. *Chem. Soc. Rev.* **2017**, *46*, 158−196.
(29) Hirsch, A. Functionalization of Single-Walled Carbon Nanotubes. *Angew. Chem., Int. Ed.* **2002**, *41*, 1853−1859.
(30) Karousis, N.; Tagmatarchis, N.; Tasis, D. Current Progress on the Chemical Modification of Carbon Nanotubes. *Chem. Rev.* **2010**, *110*, 5366−5397.
(31) Tasis, D.; Tagmatarchis, N.; Bianco, A.; Prato, M. Chemistry of Carbon Nanotubes. *Chem. Rev.* **2006**, *106*, 1105−1136.
(32) Karousis, N.; Suarez-Martinez, I.; Ewels, C. P.; Tagmatarchis, N. Structure, Properties, Functionalization, and Applications of Carbon Nanohorns. *Chem. Rev.* **2016**, *116*, 4850−4883.
(33) Georgakilas, V.; Otyepka, M.; Bourlinos, A. B.; Chandra, V.; Kim, N.; Kemp, K. C.; Hobza, P.; Zboril, R.; Kim, K. S. Functionalization of Graphene: Covalent and Non-Covalent Approaches, Derivatives and Applications. *Chem. Rev.* **2012**, *112*, 6156−6214.
(34) Georgakilas, V.; Tiwari, J. N.; Kemp, K. C.; Perman, J. A.; Bourlinos, A. B.; Kim, K. S.; Zboril, R. Noncovalent Functionalization of Graphene and Graphene Oxide for Energy Materials, Biosensing, Catalytic, and Biomedical Applications. *Chem. Rev.* **2016**, *116*, 5464−5519.
(35) Star, A.; Joshi, V.; Skarupo, S.; Thomas, D.; Gabriel, J.-C. P. Gas Sensor Array Based on Metal-Decorated Carbon Nanotubes. *J. Phys. Chem. B* **2006**, *110*, 21014−21020.
(36) Baby, T. T.; Aravind, S. S. J.; Arockiadoss, T.; Rakhi, R. B.; Ramaprabhu, S. Metal Decorated Graphene Nanosheets as Immobilization Matrix for Amperometric Glucose Biosensor. *Sens. Actuators, B* **2010**, *145*, 71−77.
(37) Kauffman, D. R.; Sorescu, D. C.; Schofield, D. P.; Allen, B. L.; Jordan, K. D.; Star, A. Understanding the Sensor Response of Metal-Decorated Carbon Nanotubes. *Nano Lett.* **2010**, *10*, 958−963.
(38) Leghrib, R.; Dufour, T.; Demoisson, F.; Claessens, N.; Reniers, F.; Llobet, E. Gas Sensing Properties of Multiwall Carbon Nanotubes Decorated with Rhodium Nanoparticles. *Sens. Actuators, B* **2011**, *160*, 974−980.
(39) Axet, M. R.; Dechy-Cabaret, O.; Durand, J.; Gouygou, M.; Serp, P. Coordination Chemistry on Carbon Surfaces. *Coord. Chem. Rev.* **2016**, *308*, 236−345.
(40) Jackson, M. N.; Surendranath, Y. Molecular Control of Heterogeneous Electrocatalysis through Graphite Conjugation. *Acc. Chem. Res.* **2019**, *52*, 3432−3441.
(41) Cho, K. Y.; Seo, H. Y.; Yeom, Y. S.; Kumar, P.; Lee, A. S.; Baek, K.-Y.; Yoon, H. G. Stable 2D-structured Supports Incorporating Ionic Block Copolymer-Wrapped Carbon Nanotubes with Graphene Oxide toward Compact Decoration of Metal Nanoparticles and High-Performance Nano-Catalysis. *Carbon* **2016**, *105*, 340−352.
(42) Wu, Y.; Jiang, Z.; Lu, X.; Liang, Y.; Wang, H. Domino Electroreduction of CO_2 to Methanol on a Molecular Catalyst. *Nature* **2019**, *575*, 639−642.
(43) Jiang, K.; Back, S.; Akey, A. J.; Xia, C.; Hu, Y.; Liang, W.; Schaak, D.; Stavitski, E.; Nørskov, J. K.; Siahrostami, S.; Wang, H. Highly Selective Oxygen Reduction to Hydrogen Peroxide on Transition Metal Single Atom Coordination. *Nat. Commun.* **2019**, *10*, 3997.
(44) Yin, P.; Yao, T.; Wu, Y.; Zheng, L.; Lin, Y.; Liu, W.; Ju, H.; Zhu, J.; Hong, X.; Deng, Z.; Zhou, G.; Wei, S.; Li, Y. Single Cobalt Atoms with Precise N-Coordination as Superior Oxygen Reduction Reaction Catalysts. *Angew. Chem., Int. Ed.* **2016**, *55*, 10800−10805.
(45) Thomas, J. M.; Raja, R.; Lewis, D. W. Single-Site Heterogeneous Catalysts. *Angew. Chem., Int. Ed.* **2005**, *44*, 6456−6482.
(46) Liu, J. Catalysis by Supported Single Metal Atoms. *ACS Catal.* **2017**, *7*, 34−59.
(47) Ramírez-Monroy, A.; Swager, T. M. Metal Chelates Based on Isoxazoline[60]fullerenes. *Organometallics* **2011**, *30*, 2464−2467.
(48) Nagai, Y.; Hirabayashi, T.; Dohmae, K.; Takagi, N.; Minami, T.; Shinjoh, H.; Matsumoto, S. i. Sintering inhibition mechanism of platinum supported on ceria-based oxide and Pt-oxide−support interaction. *J. Catal.* **2006**, *242*, 103−109.
(49) Li, G.; Jin, R. Atomically Precise Gold Nanoclusters as New Model Catalysts. *Acc. Chem. Res.* **2013**, *46*, 1749−1758.
(50) Herman, A. P.; Boncel, S. Nitrile *N*-oxides in Programmable One-Pot Functionalization of Multi-Wall Carbon Nanotubes *via* 1,3-Dipolar Cycloaddition. *RSC Adv.* **2016**, *6*, 64129−64132.
(51) Popławska, M.; Żukowska, G. Z.; Cudziło, S.; Bystrzejewski, M. Chemical Functionalization of Carbon-Encapsulated Magnetic Nanoparticles by 1,3-Dipolar Cycloaddition of Nitrile Oxide. *Carbon* **2010**, *48*, 1318−1320.
(52) Alvaro, M.; Atienzar, P.; de la Cruz, P.; Delgado, J. L.; Troiani, V.; Garcia, H.; Langa, F.; Palkar, A.; Echegoyen, L. Synthesis, Photochemistry, and Electrochemistry of Single-Wall Carbon Nanotubes with Pendent Pyridyl Groups and of Their Metal Complexes with Zinc Porphyrin. Comparison with Pyridyl-Bearing Fullerenes. *J. Am. Chem. Soc.* **2006**, *128*, 6626−6635.
(53) Uceta, H.; Vizuete, M.; Carrillo, J. R.; Barrejón, M.; Fierro, J. L. G.; Prieto, M. P.; Langa, F. Cycloaddition of Nitrile Oxides to Graphene: a Theoretical and Experimental Approach. *Chem. - Eur. J.* **2019**, *25*, 14644−14650.
(54) Hong, W. T.; Risch, M.; Stoerzinger, K. A.; Grimaud, A.; Suntivich, J.; Shao-Horn, Y. Toward the Rational Design of Non-Precious Transition Metal Oxides for Oxygen Electrocatalysis. *Energy Environ. Sci.* **2015**, *8*, 1404−1427.
(55) Han, L.; Dong, S.; Wang, E. Transition-Metal (Co, Ni, and Fe)-Based Electrocatalysts for the Water Oxidation Reaction. *Adv. Mater.* **2016**, *28*, 9266−9291.
(56) Suntivich, J.; May, K. J.; Gasteiger, H. A.; Goodenough, J. B.; Shao-Horn, Y. A Perovskite Oxide Optimized for Oxygen Evolution Catalysis from Molecular Orbital Principles. *Science* **2011**, *334*, 1383.
(57) Bergmann, A.; Jones, T. E.; Martinez Moreno, E.; Teschner, D.; Chernev, P.; Gliech, M.; Reier, T.; Dau, H.; Strasser, P. Unified Structural Motifs of the Catalytically Active State of Co(Oxyhydr)-Oxides During the Electrochemical Oxygen Evolution Reaction. *Nat. Catal.* **2018**, *1*, 711−719.
(58) Matheu, R.; Garrido-Barros, P.; Gil-Sepulcre, M.; Ertem, M. Z.; Sala, X.; Gimbert-Suriñach, C.; Llobet, A. The Development of Molecular Water Oxidation Catalysts. *Nat. Rev. Chem.* **2019**, *3*, 331−341.
(59) Garrido-Barros, P.; Gimbert-Suriñach, C.; Matheu, R.; Sala, X.; Llobet, A. How to Make an Efficient and Robust Molecular Catalyst for Water Oxidation. *Chem. Soc. Rev.* **2017**, *46*, 6088−6098.
(60) Vázquez, E.; Prato, M. Carbon Nanotubes and Microwaves: Interactions, Responses, and Applications. *ACS Nano* **2009**, *3*, 3819−3824.
(61) P. Economopoulos, S.; Karousis, N.; Rotas, G.; Pagona, G.; Tagmatarchis, N. Microwave-assisted Functionalization of Carbon Nanostructured Materials. *Curr. Org. Chem.* **2011**, *15*, 1121−1132.
(62) Delgado, J. L.; de la Cruz, P.; Langa, F.; Urbina, A.; Casado, J.; López Navarrete, J. T. Microwave-assisted sidewall functionalization of single-wall carbon nanotubes by Diels−Alder cycloaddition. *Chem. Commun.* **2004**, 1734−1735.
(63) Liu, J.; Zubiri, M. R. i.; Vigolo, B.; Dossot, M.; Fort, Y.; Ehrhardt, J.-J.; McRae, E. Efficient Microwave-Assisted Radical Functionalization of Single-Wall Carbon Nanotubes. *Carbon* **2007**, *45*, 885−891.
(64) Brunetti, F. G.; Herrero, M. A.; Muñoz, J. d. M.; Díaz-Ortiz, A.; Alfonsi, J.; Meneghetti, M.; Prato, M.; Vázquez, E. Microwave-Induced Multiple Functionalization of Carbon Nanotubes. *J. Am. Chem. Soc.* **2008**, *130*, 8094−8100.
(65) Li, J.; Grennberg, H. Microwave-Assisted Covalent Sidewall Functionalization of Multiwalled Carbon Nanotubes. *Chem. - Eur. J.* **2006**, *12*, 3869−3875.

https://doi.org/10.1021/jacs.1c05439
J. Am. Chem. Soc. 2021, 143, 10441−10453

(66) Brunetti, F. G.; Herrero, M. A.; Muñoz, J. d. M.; Giordani, S.; Díaz-Ortiz, A.; Filippone, S.; Ruaro, G.; Meneghetti, M.; Prato, M.; Vázquez, E. Reversible Microwave-Assisted Cycloaddition of Aziridines to Carbon Nanotubes. *J. Am. Chem. Soc.* **2007**, *129*, 14580−14581.
(67) Curran, D. P.; Fenk, C. J. Thermolysis of Bis[2-[(trimethylsilyl)oxy]propyl]furoxan (TOP-furoxan). The First Practical Method for Intermolecular Cycloaddition of an *in situ* Generated Nitrile Oxide with 1,2-Di- and Trisubstituted Olefins. *J. Am. Chem. Soc.* **1985**, *107*, 6023−6028.
(68) Whitney, R. A.; Nicholas, E. S. Furoxans as Nitrile Oxide Precursors: Cycloaddition Reactions of Bis(benzenesulfonyl)-furoxan. *Tetrahedron Lett.* **1981**, *22*, 3371−3374.
(69) Rebelo, S. L. H.; Guedes, A.; Szefczyk, M. E.; Pereira, A. M.; Araújo, J. P.; Freire, C. Progress in the Raman Spectra Analysis of Covalently Functionalized Multiwalled Carbon Nanotubes: Unraveling Disorder in Graphitic Materials. *Phys. Chem. Chem. Phys.* **2016**, *18*, 12784−12796.
(70) Dresselhaus, M. S.; Dresselhaus, G.; Jorio, A.; Souza Filho, A. G.; Saito, R. Raman Spectroscopy on Isolated Single Wall Carbon Nanotubes. *Carbon* **2002**, *40*, 2043−2061.
(71) Rao, A. M.; Eklund, P. C.; Bandow, S.; Thess, A.; Smalley, R. E. Evidence for Charge Transfer in Doped Carbon Nanotube Bundles from Raman Scattering. *Nature* **1997**, *388*, 257−259.
(72) Arrigo, R.; Hävecker, M.; Wrabetz, S.; Blume, R.; Lerch, M.; McGregor, J.; Parrott, E. P. J.; Zeitler, J. A.; Gladden, L. F.; Knop-Gericke, A.; Schlögl, R.; Su, D. S. Tuning the Acid/Base Properties of Nanocarbons by Functionalization Via Amination. *J. Am. Chem. Soc.* **2010**, *132*, 9616−9630.
(73) Belu, A. M.; Graham, D. J.; Castner, D. G. Time-of-Flight Secondary Ion Mass Spectrometry: Techniques and Applications for the Characterization of Biomaterial Surfaces. *Biomaterials* **2003**, *24*, 3635−3653.
(74) Oh, S.; Bisbey, R. P.; Gul, S.; Yano, J.; Fisher, G. L.; Surendranath, Y. N-Heterocyclic Linkages Are Produced from Condensation of Amidines onto Graphitic Carbon. *Chem. Mater.* **2020**, *32*, 8512−8521.
(75) Ferrari, A. C.; Meyer, J. C.; Scardaci, V.; Casiraghi, C.; Lazzeri, M.; Mauri, F.; Piscanec, S.; Jiang, D.; Novoselov, K. S.; Roth, S.; Geim, A. K. Raman Spectrum of Graphene and Graphene Layers. *Phys. Rev. Lett.* **2006**, *97*, 187401.
(76) Criado, A.; Melchionna, M.; Marchesan, S.; Prato, M. The Covalent Functionalization of Graphene on Substrates. *Angew. Chem., Int. Ed.* **2015**, *54*, 10734−10750.
(77) Eigler, S.; Hirsch, A. Chemistry with Graphene and Graphene Oxide—Challenges for Synthetic Chemists. *Angew. Chem., Int. Ed.* **2014**, *53*, 7720−7738.
(78) Kim, Y.-T.; Tadai, K.; Mitani, T. Highly Dispersed Ruthenium Oxide Nanoparticles on Carboxylated Carbon Nanotubes for Supercapacitor Electrode Materials. *J. Mater. Chem.* **2005**, *15*, 4914−4921.
(79) Choi, H. C.; Shim, M.; Bangsaruntip, S.; Dai, H. Spontaneous Reduction of Metal Ions on the Sidewalls of Carbon Nanotubes. *J. Am. Chem. Soc.* **2002**, *124*, 9058−9059.
(80) Zakharova, I. A.; Salyn, J. V.; Tatjanenko, L. V.; Mashkovsky, Y. S.; Ponticelli, G. Inhibitory Activity of Palladium(II) and Platinum(II) Complexes with Isoxazole and its Derivatives. *J. Inorg. Biochem.* **1981**, *15*, 89−92.
(81) Yoshida, T. An X-Ray Photoelectron Spectroscopic Study of Several Ligands in Coordination Compounds. *Bull. Chem. Soc. Jpn.* **1980**, *53*, 1327−1330.
(82) Boukhvalov, D. W. DFT Modeling of the Covalent Functionalization of Graphene: From Ideal to Realistic Models. *RSC Adv.* **2013**, *3*, 7150−7159.
(83) Plasser, F.; Pašalić, H.; Gerzabek, M. H.; Libisch, F.; Reiter, R.; Burgdörfer, J.; Müller, T.; Shepard, R.; Lischka, H. The Multiradical Character of One- and Two-Dimensional Graphene Nanoribbons. *Angew. Chem., Int. Ed.* **2013**, *52*, 2581−2584.
(84) Bendikov, M.; Duong, H. M.; Starkey, K.; Houk, K. N.; Carter, E. A.; Wudl, F. Oligoacenes: Theoretical Prediction of Open-Shell Singlet Diradical Ground States. *J. Am. Chem. Soc.* **2004**, *126*, 7416−7417.
(85) Bian, S.; Scott, A. M.; Cao, Y.; Liang, Y.; Osuna, S.; Houk, K. N.; Braunschweig, A. B. Covalently Patterned Graphene Surfaces by a Force-Accelerated Diels−Alder Reaction. *J. Am. Chem. Soc.* **2013**, *135*, 9240−9243.
(86) Lu, X.; Yim, W.-L.; Suryanto, B. H. R.; Zhao, C. Electrocatalytic Oxygen Evolution at Surface-Oxidized Multiwall Carbon Nanotubes. *J. Am. Chem. Soc.* **2015**, *137*, 2901−2907.
(87) Hoque, M. A.; Gil-Sepulcre, M.; de Aguirre, A.; Elemans, J. A. A. W.; Moonshiram, D.; Matheu, R.; Shi, Y.; Benet-Buchholz, J.; Sala, X.; Malfois, M.; Solano, E.; Lim, J.; Garzón-Manjón, A.; Scheu, C.; Lanza, M.; Maseras, F.; Gimbert-Suriñach, C.; Llobet, A. Water Oxidation Electrocatalysis Using Ruthenium Coordination Oligomers Adsorbed on Multiwalled Carbon Nanotubes. *Nat. Chem.* **2020**, *12*, 1060−1066.
(88) Gong, M.; Li, Y.; Wang, H.; Liang, Y.; Wu, J. Z.; Zhou, J.; Wang, J.; Regier, T.; Wei, F.; Dai, H. An Advanced Ni−Fe Layered Double Hydroxide Electrocatalyst for Water Oxidation. *J. Am. Chem. Soc.* **2013**, *135*, 8452−8455.
(89) deKrafft, K. E.; Wang, C.; Xie, Z.; Su, X.; Hinds, B. J.; Lin, W. Electrochemical Water Oxidation with Carbon-Grafted Iridium Complexes. *ACS Appl. Mater. Interfaces* **2012**, *4*, 608−613.
(90) Tavakkoli, M.; Nosek, M.; Sainio, J.; Davodi, F.; Kallio, T.; Joensuu, P. M.; Laasonen, K. Functionalized Carbon Nanotubes with Ni(II) Bipyridine Complexes as Efficient Catalysts for the Alkaline Oxygen Evolution Reaction. *ACS Catal.* **2017**, *7*, 8033−8041.
(91) Lin, Y.; Wu, K.-H.; Lu, Q.; Gu, Q.; Zhang, L.; Zhang, B.; Su, D.; Plodinec, M.; Schlögl, R.; Heumann, S. Electrocatalytic Water Oxidation at Quinone-on-Carbon: A Model System Study. *J. Am. Chem. Soc.* **2018**, *140*, 14717−14724.
(92) Wang, L.; Chen, H.; Daniel, Q.; Duan, L.; Philippe, B.; Yang, Y.; Rensmo, H.; Sun, L. Promoting the Water Oxidation Catalysis by Synergistic Interactions between $Ni(OH)_2$ and Carbon Nanotubes. *Adv. Energy Mater.* **2016**, *6*, 1600516.
(93) Qu, K.; Zheng, Y.; Jiao, Y.; Zhang, X.; Dai, S.; Qiao, S.-Z. Polydopamine-Inspired, Dual Heteroatom-Doped Carbon Nanotubes for Highly Efficient Overall Water Splitting. *Adv. Energy Mater.* **2017**, *7*, 1602068.
(94) Lin, Y.-C.; Chuang, C.-H.; Hsiao, L.-Y.; Yeh, M.-H.; Ho, K.-C. Oxygen Plasma Activation of Carbon Nanotubes-Interconnected Prussian Blue Analogue for Oxygen Evolution Reaction. *ACS Appl. Mater. Interfaces* **2020**, *12*, 42634−42643.
(95) Malara, F.; Carallo, S.; Rotunno, E.; Lazzarini, L.; Piperopoulos, E.; Milone, C.; Naldoni, A. A Flexible Electrode Based on Al-Doped Nickel Hydroxide Wrapped around a Carbon Nanotube Forest for Efficient Oxygen Evolution. *ACS Catal.* **2017**, *7*, 4786−4795.
(96) Blakemore, J. D.; Crabtree, R. H.; Brudvig, G. W. Molecular Catalysts for Water Oxidation. *Chem. Rev.* **2015**, *115*, 12974−13005.
(97) Hull, J. F.; Balcells, D.; Blakemore, J. D.; Incarvito, C. D.; Eisenstein, O.; Brudvig, G. W.; Crabtree, R. H. Highly Active and Robust Cp* Iridium Complexes for Catalytic Water Oxidation. *J. Am. Chem. Soc.* **2009**, *131*, 8730−8731.
(98) Savini, A.; Bellachioma, G.; Ciancaleoni, G.; Zuccaccia, C.; Zuccaccia, D.; Macchioni, A. Iridium(Iii) Molecular Catalysts for Water Oxidation: The Simpler the Faster. *Chem. Commun.* **2010**, *46*, 9218−9219.
(99) Thomsen, J. M.; Huang, D. L.; Crabtree, R. H.; Brudvig, G. W. Iridium-Based Complexes for Water Oxidation. *Dalton Trans.* **2015**, *44*, 12452−12472.
(100) Thomsen, J. M.; Sheehan, S. W.; Hashmi, S. M.; Campos, J.; Hintermair, U.; Crabtree, R. H.; Brudvig, G. W. Electrochemical Activation of Cp* Iridium Complexes for Electrode-Driven Water-Oxidation Catalysis. *J. Am. Chem. Soc.* **2014**, *136*, 13826−13834.
(101) Blakemore, J. D.; Schley, N. D.; Balcells, D.; Hull, J. F.; Olack, G. W.; Incarvito, C. D.; Eisenstein, O.; Brudvig, G. W.; Crabtree, R.

https://doi.org/10.1021/jacs.1c05439
J. Am. Chem. Soc. 2021, 143, 10441−10453

H. Half-Sandwich Iridium Complexes for Homogeneous Water-Oxidation Catalysis. *J. Am. Chem. Soc.* **2010**, *132*, 16017−16029.
(102) Gong, M.; Dai, H. A Mini Review of NiFe-Based Materials as Highly Active Oxygen Evolution Reaction Electrocatalysts. *Nano Res.* **2015**, *8*, 23−39.
(103) Yin, Q.; Tan, J. M.; Besson, C.; Geletii, Y. V.; Musaev, D. G.; Kuznetsov, A. E.; Luo, Z.; Hardcastle, K. I.; Hill, C. L. A Fast Soluble Carbon-Free Molecular Water Oxidation Catalyst Based on Abundant Metals. *Science* **2010**, *328*, 342.
(104) Diaz-Morales, O.; Ferrus-Suspedra, D.; Koper, M. T. M. The Importance of Nickel Oxyhydroxide Deprotonation on Its Activity Towards Electrochemical Water Oxidation. *Chem. Sci.* **2016**, *7*, 2639−2645.
(105) Görlin, M.; Chernev, P.; Ferreira de Araújo, J.; Reier, T.; Dresp, S.; Paul, B.; Krähnert, R.; Dau, H.; Strasser, P. Oxygen Evolution Reaction Dynamics, Faradaic Charge Efficiency, and the Active Metal Redox States of Ni−Fe Oxide Water Splitting Electrocatalysts. *J. Am. Chem. Soc.* **2016**, *138*, 5603−5614.
(106) Hall, D. S.; Lockwood, D. J.; Bock, C.; MacDougall, B. R. Nickel Hydroxides and Related Materials: A Review of Their Structures, Synthesis and Properties. *Proc. R. Soc. London, Ser. A* **2015**, *471*, 20140792.
(107) McDaniel, N. D.; Coughlin, F. J.; Tinker, L. L.; Bernhard, S. Cyclometalated Iridium(III) Aquo Complexes: Efficient and Tunable Catalysts for the Homogeneous Oxidation of Water. *J. Am. Chem. Soc.* **2008**, *130*, 210−217.
(108) Miró, P.; Ertem, M. Z.; Gagliardi, L.; Cramer, C. J. Quantum Chemical Characterization of Water Oxidation Catalysts. In *Molecular Water Oxidation Catalysis*; Llobet, A., Ed.; Wiley: 2014; pp 233−255.
(109) Garrido-Barros, P.; Matheu, R.; Gimbert-Suriñach, C.; Llobet, A. Electronic, Mechanistic, and Structural Factors That Influence the Performance of Molecular Water Oxidation Catalysts Anchored on Electrode Surfaces. *Curr. Opin. Electrochem.* **2019**, *15*, 140−147.
(110) Sala, X.; Maji, S.; Bofill, R.; García-Antón, J.; Escriche, L.; Llobet, A. Molecular Water Oxidation Mechanisms Followed by Transition Metals: State of the Art. *Acc. Chem. Res.* **2014**, *47*, 504−516.
(111) Liao, R.-Z.; Siegbahn, P. E. M. Quantum Chemical Modeling of Homogeneous Water Oxidation Catalysis. *ChemSusChem* **2017**, *10*, 4236−4263.
(112) Vilella, L.; Vidossich, P.; Balcells, D.; Lledós, A. Basic Ancillary Ligands Promote O−O Bond Formation in Iridium-Catalyzed Water Oxidation: A Dft Study. *Dalton Trans.* **2011**, *40*, 11241−11247.

https://doi.org/10.1021/jacs.1c05439
J. Am. Chem. Soc. 2021, 143, 10441−10453